Supplementary Information

Cloud droplet activation of secondary organic aerosol is mainly controlled by molecular weight, not water solubility

Jian Wang, John E. Shilling, Jiumeng Liu, Alla Zelenyuk, David M. Bell, Markus Petters, Ryan Thalman, Fan Mei, Rahul A. Zaveri, and Guangjie Zheng

1. Experimental setup

1.1 Steady state chamber experiments

Experiments were conducted in Pacific Northwest National Laboratory's 10.6 m^3 environmental chamber under a wide range of conditions. Experiments were run in the continuous-flow mode, where reactants are continuously injected into the chamber and are oxidized as they flow through it. Total flow rate through the chamber for these experiments varied between 35.7 and 48.3 l min^{-1} resulting in mean residence times of 3.7 – 4.9 hours. Effloresced ammonium sulfate particles were generated by atomizing dilute solutions of ammonium sulfate and passing the aerosol through a custom designed diffusion dryer, which was 1.83 meter long with inner diameter of 10.2 cm. The sulfate particles were then size selected at 50 nm by a differential mobility analyzer (DMA, Model 3081, TSI Inc.) operating at a sheath to aerosol flow ratio of 10:3.2 before injected into the chamber. Measurements of the size-selected seed particles by a downstream SMPS confirmed their phase state and size. Water vapor was injected into the chamber by passing an air flow through a stainless steel bubbler containing 18.2 MΩ cm MilliQ water. The flow through the bubbler was continuously varied to maintain the target RH using a feedback-control loop. VOCs were introduced into the chamber using one of two methods. Isoprene and α-pinene were continuously injected into the chamber from gas

cylinders at rates controlled by a mass flow controller. β-caryophyllene, Δ-3 carene, and toluene were injected into the chamber by flowing pure air at a constant rate through a bulb containing a few drops of the pure liquid and immersed in a constant temperature bath held at 5 °C. Hydrogen peroxide was added to the chamber by injecting it into a gently warmed bulb using a syringe pump and sweeping the vapor into the chamber in a flow of pure air. When desired, NO was injected into the chamber from a gas cylinder using a mass flow controller, and O_3 was generated and introduced into the chamber by passing pure air over a Jelight model 600 ozone lamp.

Chamber RH and temperature were measured with a Rotronic SC05 sensor. UV-light was provided by 104 Q-Labs UVA-340 blacklights surrounding the chamber and its intensity in the chamber was measured in real-time using a J_{NO2} radiometer and measured J_{NO2}=0.2 hr^{-1}. Photolysis of H_2O_2 generated OH radical for oxidation. The radiometer measurements agreed with measurements using the photostationary state method (Holmes et al., 1973). Ozone concentrations in the chamber were monitored using a Thermo Scientific model 49i ozone sensor. NO/NOx concentrations were measured using a Thermo Scientific 42i detector. Particle size distributions were measured using scanning mobility particle sizer (SMPS) consisting of a TSI 3080 long-column DMA and a TSI 3775 CPC. Aerosol chemical composition was characterized using an Aerodyne HR-ToF-AMS (DeCarlo et al., 2006). The instrument was regularly calibrated during the experiments and data were analyzed using standard methods described in the literature (Allan et al., 2004). The collection efficiency of the AMS varied between 1 and 0.5, depending on the SOA precursor, and the relative inonization efficiency of organics was 1.4. The values of O:C and H:C were calculated using the updated fragmentation tables in Canagaratna et al. (2015). for all SOA precursors except for isoprene, which used the fragmentation tables of Chen et al. (2011). VOCs were measured using an Ionicon quadrupole

PTR-MS (Lindinger et al., 1998). The PTR-MS was regularly calibrated using a certified gas cylinder containing most of the experimental gases. Δ-3 carene and β-caryophyllene concentrations were approximated using the response factor for α-pinene. The experimental conditions are listed in Table S1 (Supplementary Information).

1.2 Size-resolved CCN measurements

The size-resolved CCN activated fraction was measured using the same system and approach described in Mei et al. (2013) and is briefly described here. Aerosol particles from the steady state chamber were first dried to below 20% relative humidity (RH), neutralized by a Kr-85 aerosol neutralizer, and subsequently classified by a DMA. The classified aerosol was then simultaneously characterized by a condensation particle counter and a CCN counter (Model CCN-100, Droplet Measurement Technologies, Inc.). The sample and sheath flows of the DMA were maintained at 0.89 and 8.9 L min^{-1}, respectively. The total flow of CPC was reduced to 0.39 L min^{-1} and the sample flow of the CCN counter was maintained at 0.5 L min^{-1}.

The longitudinal temperature gradient of the CCN counter was stepped through 4.55, 4.7, 4.85, 5.0, 5.3, 5.5, 5.65, 6.0, 6.4, 6.9, 7.8, 8.5, 9.3 ˚C, which corresponded to supersaturations (*S*) ranging from ~0.1% to ~0.6%. The supersaturation inside the CCN counter was maintained at each value for approximately 8 minutes, during which the diameter of particles classified by the DMA was scanned between 30 nm and 315 nm twice, with each scan lasting 180 seconds . Immediately following each change of temperature gradient (i.e., supersaturation), the system waited for 90 seconds to ensure that the temperatures stabilized before the next scan of particle size commenced. The CCN counter was stepped through the above 13 *S* values approximately every 100 minutes. The aerosol size distribution was derived by inverting the particle

concentration measured by the CPC using a routine described in Collins et al. (2002). The same procedure was also applied to the measured CCN concentration to obtain CCN size distribution. The ratio of the inverted CCN and aerosol size distributions provided size-resolved CCN activated fraction.

The CCN counter was calibrated at the 0.5 L min^{-1} sampling flow rate, and under the 13 temperature gradients using ammonium sulfate particles before and after the experiments during the summer of 2015 and again before and after the experiments in February of 2016. The instrument supersaturation was derived from Köhler theory using a constant van't Hoff factor of 2.5 for ammonium sulfate. Since both sample pressure and temperature were essentially identical during measurements and calibrations, no temperature or pressure correction of the calibrated supersaturation is necessary.

We note some of the volatile SOA species may evaporate as a result of the heating inside CCN counter growth column (e.g., Asa-Awuku et al., 2009). However, CCN are quickly activated inside the growth column (i.e., within 10 seconds), and once activated, the evaporation of volatile species is likely slow. As the CCN remains un-activated near the top of the growth column, where temperature is very close to the room temperature, we expect overall effect on CCN measurements due to the evaporation is minor. Co-condensation of water soluble vapors during droplet growth lowers the supersaturation required for CCN activation (Topping et al., 2013). On the other hand, because the surface area of the wetted growth column inner wall is much larger than that of the activating particles, vast majority of the water soluble vapors is expected to be uptaken by the wetted innner wall, therefore the effect of co-condensation on measurements by the CCN counter is expected to be minimal.

2. Uncertainty of derived effective organic hygroscopicity

As organic particles formed by condensational growth of ammonium sulfate seeds are spherical (Zelenyuk et al., 2008b), no shape factor correction is necessary for the derivation of particle κ from the measured particles sizes. The impact of coagulation is minor under the experimental conditions. The value of κ_{org} was derived from Eq. 1 in the main text, therefore its uncertainty derives from the uncertainties of particle κ and sulfate volume fraction. As particle κ was derived from the activation spectrum (the variation of activated fraction as a function of supersaturation) of size-selected particles, the uncertainty in particle κ can be attributed to the uncertainties in particles size, supersaturation of CCN counter, and activation fractions. The uncertainty in sulfate volume fraction derives from the uncertainties in the mode diameters of ammonium sulfate seeds and grown particles size-selected for CCN measurements.

Given the steps involved in the derivation of κ_{org}, it is difficult to obtain the uncertainty of κ_{org} analytically through error propagation. Instead, the uncertainty was calculated numerically using a Monte Carlo approach described as follows. The CCN counter supersaturation, activation fraction, and the mode diameters of ammonium sulfate seeds and grown particles size-selected for CCN measurements were randomly chosen from normal distributions with respective mean values and standard deviations. These randomly chosen parameters were then used to calculate κ_{org} following the method described in the main text. The above calculation was repeated 100 times, and the uncertainty of κ_{org} was derived from the distribution of the 100 κ_{org} values. The distribution of CCN counter supersaturation was assumed as a normal distribution, and the mean and standard deviation of the distribution was derived from the repeated calibration values (e.g., Fig. 1 in the main text). The mode diameter of ammonium sulfate seeds, the mode diameter of grown particles size-selected for CCN measurements, and the activated fraction were assumed to

have normal distributions with standard deviations as 1%, 1%, and 5% of the mean values, respectively.

3. Impact of particles grown from doubly charged seeds on derived organic hygroscopicity

In addition to the singly-charged 50 nm ammonium sulfate (AS) seeds, the DMA also selects doubly-charged AS particles with a mode dimeter of 72.6 nm. Particles grown on the doubly charged seeds have a higher sulfate volume fraction compared to those of the same size but grown on singly charged seeds, therefore higher particle hygroscopicity. The derivation of particle κ and κ_{org} therefore requires the knowledge of the fraction of particles grown from doubly charged seeds. Let $n_{1,0}(D_p)$ and $n_{2,0}(D_p)$ represent the size distribution of singly and doubly charged ammonium sulfate seeds introduced into the chamber, and $n_1(D_p)$ and $n_2(D_p)$ represent particles exiting the chamber that are grown on the singly and doubly charged seeds, respectively. The fraction of sampled particles that are grown from doubly charged seeds, $f_2(D_p)$ is given by $f_2(D_p) = n_2(D_p) \Big/ \left(n_1(D_p) + n_2(D_p) \right)$. Figure S2 shows an example of the seed particle size distribution measured on July 10th, 2015, $n_{1,0}$ and $n_{2,0}$ were derived by fitting the measured size distribution using lognormal modes. The result shows that the population of doubly charged seeds represented a very minor (number) fraction of the total seeds introduced into the chamber.

The fraction of particles grown from doubly charged seeds and its variation with particle diameter are influenced by several factors and are difficult to obtain based on calculations alone. In this study, we derive $f_2(D_p)$ by combining direct measurements of $f_2(D_p)$ at 100 nm and simulated spectral profile of $f_2(D_p)$. The procedure is detailed below. For grown particles that are

size-selected at 100 nm, there are two populations, one with singly charged AS seed and a nominal 25 nm thick SOA coating, and others with doubly charged AS seed and a 13.7 nm thick SOA coating. These particles have essentially the same mobility diameter, but different densities, and thus different vacuum aerodynamic diameters (D_{va}) (Zelenyuk et al., 2008a). Having the same mobility diameters and spherical shape, the detection efficiency of these two particle types is identical, as is the transmission through the inlet of single particle mass spectrometer, miniSPLAT (Zelenyuk et al., 2015), used to measure their D_{va}, shape, density, and composition. Figure S3 provides, an example, D_{va} distributions of SOA-coated AS particles classified with mobility diameters of 100 nm. The first peak corresponds to particles with lower density, containing singly charged AS seeds, while the second peak is of particles grown on doubly charged AS seeds. Also shown is the fit of the data with two peaks. The value of $f_2(D_p)$ at 100 nm can be straightforwardly derived from the areas of the two peaks that reflect the relative abundance of two particle populations in the sample.

To obtain the spectral profile of $f_2(D_p)$, we first simulate the size distributions of particles grown from singly and double seeds from $n_{1,0}$ and $n_{2,0}$ using a model presented in Seinfeld et al. (2003). In this model, particle growth is treated as condensation of two empirical species, and the growth rate is expressed as:

$$I(D_p) = \frac{dD_p}{dt} = \beta_A \frac{f(Kn_A)}{D_p} + \beta_B \frac{f(Kn_B)}{D_p} \quad \text{(S1)}$$

Where β_i is related to the product of the molecular diffusivity, molecular weight, and the vapor pressure difference between the surrounding atmosphere and that above the particle surface for species *i*, and

$$f(Kn_i) = f\left(\frac{\lambda_i}{D_p}\right) = \frac{1}{1+\frac{\lambda_i}{D_p}} \quad \text{(S2)}$$

where λ_i is the mean free path of species *i*. With the four parameters β_A, β_B, λ_A, and λ_B, mean residence time of particles in the chamber (τ), and particle wall loss coefficient (α), we can derive $n_1(D_p)$ and $n_2(D_p)$ and therefore $f_2(D_p)$ from $n_{1,0}(D_p)$ and $n_{2,0}(D_p)$ using the model. The mean residence time ranged from 3.7 to 4.9 hours for the experiments. Figure S4 shows $f_2(D_p)$ as a function of D_p derived from seed particle size distributions shown in Fig. S2 using τ of 4.3 hours, and a set of representative parameters (i.e., α = 0.027 h^{-1}, β_A=1.5×10^{-6} $\mu m^2 s^{-1}$, β_B=2.5×10^{-7} $\mu m^2 s^{-1}$, λ_A = 17 nm, and λ_A = 21 nm) reported in Seinfeld et al. (2003). $f_2(D_p)$ starts with a low value (~ 2%) at 52 nm, and it increases with D_p, and reaches a plateau of 18% at ~ 100 nm.

To examine the dependence of $f_2(D_p)$ spectral profile on model parameters, we introduce a normalized $f_2(D_p)$ as:

$$\overline{f_2(D_p)} = f_2(D_p) \Big/ \max\left[f_2(D_p) \right]$$

The dependences of $\overline{f_2(D_p)}$ on α, β_i, λ_i values are shown in Fig. S5. $\overline{f_2(D_p)}$ shows negligible variation for two orders of magnitude change in α, β_i, or λ_i. The profiles consistently show that $f_2(D_p)$ reaches its plateau at ~100 nm. Therefore, we combine $\overline{f_2(D_p)}$ and f_2 measured at 100 nm to derive f_2 at the size of particles sampled by the size resolved CCN system.

At a given particle size, the influence of particles grown from doubly charged seeds on derived κ_{org} is taken into consideration using the following approach. Particles grown from doubly charged seeds have higher sulfate volume fraction, and therefore low critical supersaturation. Let S_c denote the critical supersaturation for size-selected particles grown from

singly-charged 50 nm seeds. Assuming particles grown from double charged particles are all activated at S_c due to their higher hygroscopicity, we derive S_c as the supersaturation at which the activated fraction reaches 50%×(1- f_2) + f_2 = 50%× (1+ f_2). The overall particle κ is then derived from particle diameter and S_c using the approached described in earlier papers (e.g., Mei et al., 2013). For the isoprene and monoterpene experiments, the average f_2 at 100 nm was 15% with a standard deviation of 5%. For the β-caryophyllene experiment, f_2 at 100 nm was measured as 5% while no data were available for the Toluene experiment. In this study, we used 15% for f_2 at 100 nm for isoprene and monoterpene experiments, and 5% for β-caryophyllene and toluene experiments. Changing f_2 at 100 nm for the isoprene and monoterpene experiments to 10% or 26% (i.e., minimum and maximum measured during these experiments) or changing f_2 at 100 nm to 2.5% or 10% for the β-caryophyllene and toluene experiments leads negligible change in the trend of κ_{org} with x_{AS} shown in Fig. 1 and Fig. S1.

4. Examples of Köhler curve for mixtures of sulfate and sparingly soluble organics

The Köhler curve (blue line in Fig. S6) was calculated for mixtures of ammonium sulfate and sparing soluble organics with solubility C of 0.01. The volume of sulfate inside the particles is equivalent to a 50 nm sulfate particle, same as particles formed in the steady state chamber. As the droplets grow, and fraction of dissolved organics increases, eventually reaches 100% (Fig. S5). This gradual increase of h leads to two (local) maxima of the Köhler curve (Fig. S6). The relative magnitude of the supersaturation maxima varies with the volume fraction of the sparingly soluble organics. For particles with sulfate volume fraction of 0.1 (diameter of 108 nm), the first maximum dominates and represents the critical supersaturation of 0.29%, at which

point 32% of the sparingly soluble organics are dissolved. For particle with sulfate volume fraction of 0.2, the 2nd maximum becomes the highest point of the Köhler curve at 0.32%. In this case, all organics are dissolved at the point of activation, and the effective organic hygroscopicity is the same as the intrinsic organic hygroscopicity, therefore not limited by the organic water solubility.

5. Simulation of κ_{org} for particles consisting of organics with a distribution of solubility

The effective organic hygroscopicity κ_{org} were also simulated for particles composed of ammonium sulfate seed and model organic compounds with $\kappa_{org,\ intr}$ of 0.15 and various assumptions of the solubility distribution. The results are shown in Fig. S7. For these simulations, 61 compounds were used. All compounds have the same $\kappa_{org,\ intr}$ = 0.15 and their water solubility is lognormally distributed as shown in panels (b), (d), and (f). Each bin represents a compound and the fraction of each bin in the plotted distribution corresponds to the volume fraction of the compound with the corresponding solubility in the organic phase. The mode of the solubility distribution is fixed according to the isolines selected for simulations in panels (a), (c), and (e), with the mode solubility C_m varying from 5×10^{-2} to 1×10^{-5}. The top row corresponds to a geometric standard deviation σ_g = 1 for the solubility distribution. This simulation corresponds to the single solubility simulation shown Fig. 2 of the main text. The second row corresponds to a narrower set of solubility distributions with σ_g = 2 and the bottom row to wider set of solubility distributions with σ_g = 3. The dissolution of each organic compound is assumed not affected by the presence of other organics in the particle phase for the simulations.

Figure S7 shows how changing from a single organic compound to a multicomponent mixture with distributed solubility affects the x_{AS} value where the simulated κ_{org} approaches the plateau at the intrinsic $\kappa_{org,\ intr}$. The wider the distribution, the lower is the x_{AS} where the plateau is reached for selected mode solubility. This is partially due to the right tail of the solubility distribution. These compounds are more soluble than the mode solubility and therefore dissolve at lower water contents. Not unexpectedly the entire aerosol is more easily dissolved in the distributed simulations. One peculiar case is the $C = 10^{-3}$ simulation shown in Fig. S7 (e). At low x_{AS}, the addition of sulfate appears to make the aerosol less soluble, manifesting itself in a decrease in κ_{org}. At first glance this should not occur, as adding ammonium sulfate should always add additional water that aides the dissolution of the organics. One hidden feature in these simulations is that the particle size is not constant. Volume fraction is varied by starting with a 50 nm AS core and high organic fractions are achieved by very thick coatings of organic material. This implies that increasing x_{AS} corresponds to decreasing particle size in the simulations. Generally, this has only a small influence on the result. However, in cases where the solubility is just right, the increasing Kelvin effect can decrease the total particle water content and thus compensate for the increasing water content by the added sulfate. This explains the dip in the $C = 10^{-3}$ simulation in Fig. S6 (e). This behavior occurs in a very narrow range of solubility that is unlikely replicable in actual experiments. The general conclusion from these simulations is that the broader the distribution of solubility, the more the sparingly soluble range is shifted toward lower solubilities. Compounds with $C < 1\times10^{-5}$ remain effectively insoluble, except when present in predominately inorganic particle matrices.

6. Solubility, miscibility, liquid-liquid phase separation, and CCN activation

Solubility refers to the amount of material present in the saturated solution. For an initially dry particle, solubility and water activity of the saturated solution will control the size and RH at which pure crystalline substances spontaneously dissolve (Bilde and Svenningsson, 2004; Hori et al., 2003; Petters and Kreidenweis, 2008; Shulman et al., 1996). For particles that include sparingly soluble compounds, the dissolution occurs in the supersaturated regime and thereby exerts some control over the critical supersaturation. This gives rise to strong sensitivity of κ_{org} with increasing inorganic fraction. Miscibility is related to solubility and refers to the ability of two liquid phases to mix. Substances that form two liquid phases are immiscible. If a miscibility transition occurs in the supersaturated regime, miscibility limitations exert a similar control over critical supersaturation as solubility (Petters et al., 2006; Petters et al., 2016), i.e., the effective hygroscopicity κ_{org} observed from CCN activation is reduced at lower net water contents (smaller size or less hygroscopic material present). Distinguishing between miscibility and solubility in CCN experiments is not possible because the manifestation of the effect is identical.

In general, SOA precursors are weakly oxidized hydrocarbons. These hydrocarbons are liquid if present in the condensed phase and immiscible with water. Oxidation of the precursor adds functional groups to the compounds. These functional groups lower the vapor pressure and increase viscosity (Rothfuss and Petters, 2017), density (Kuwata et al., 2012), and miscibility (Petters et al., 2016). Model calculations and experimental data suggest that at O:C ratios of 0.5 or higher, miscibility limitations become negligible for compounds that are composed of hydroxyl and/or acid groups (Bertram et al., 2011; Petters et al., 2016).

7. Solubility, surface tension, and CCN activation

One hypothesis for the observed near constant κ_{org} is that surface tension and solubility effects conspire to produce this result. Here we use simulations to demonstrate how model predictions would change if the organic phase was strongly surface active. To do so, we combine the models of Petters and Kreidenweis (2008, 2013) that treat limited solubility and the surface tension reduction. The model equations are taken from the original publications and are summarized in Table S2. Key model parameters are listed in Table S3. Sorption isotherms for the systems studied here are not available. Therefore, model calculations were performed for a series of hypothetical sorption isotherms assuming molar volume $\alpha = 1.8 \times 10^{-4}\, m^3\, mol^{-1}$, surface excess $\Gamma_{max} = 5 \times 10^{-6}\, mol\, m^{-2}$, inverse activity coefficient $\beta = \{0.1, 10, 1000\}\, mol\, m^{-3}$, and critical micelle concentration $cmc = 0.03\, J\, m^{-2}$. The molar volume corresponds to a $\kappa_{org,intr}$ value of 0.1. A detailed literature review of sorption isotherms for several compounds is provided in Fig. 1 of Petters and Petters (2016). Figure S8 (a) illustrates the assumed isotherms for the simulations here. The three model sorption isotherms circumscribe scenarios of strong and weak surface activities. The range of water content at the point of activation is computed as in Petters and Petters (2016) and indicated on the graph. The critical micelle concentration determines the lowest possible surface tension of the solutions. The value of 0.03 J m^{-2} was selected to approximately correspond to typical values found for surfactants (see Fig. 1 of Petters and Petters, 2016). Simulations were also performed for a range of assumed solubilities spanning $C = \{\infty, 0.01, 0.001\}$. Reference calculations for the surface tension of pure water, $\sigma = 0.072\, J\, m^{-2}$, are also included. All calculations were performed starting with a 50 nm AS core particle and varying over a range of organic coating thickness corresponding to 70 – 300 nm grown particle diameter, as in the calculations shown in Fig. 2.

Figure S8 demonstrates that for a non-dissociating surfactant, the predicted κ_{org} is similar to the values predicted assuming the surface tension of pure water. This is because partitioning to the surface results in loss of bulk water, which reduces the water content relative to the reference case of no surface tension reduction. Note that this behavior is consistent with experimental CCN data for pure and internally mixed surfactants (Petters and Petters, 2016; Prisle et al., 2010). The model calculations show that treating the organic phase as surface active will not alter the solubility signature shown in Fig. 2 of the main text.

We note that the interplay of solubility, liquid-liquid phase separation, and surface tension during activation remains poorly understood. Several new mechanisms have been proposed (Noziere et al., 2014; Ovadnevaite et al., 2017; Ruehl et al., 2016), however, limited data are available to test these to date. Using measurements at Mace Head, Ovadnevaite et al. (2017) showed that for most of the time, calculated CCN concentration assuming a surface tension of water agreed well with the measured. However, during periods when organics were mixed with inorganic salt solutions in nascent ultrafine mode (i.e., particle diameter between 10 nm and 50 nm), the measured CCN concentration was significantly higher than the calculation based on measured chemical composition and the surface tension of water, but could be reproduced by assuming a much lower surface tension of ~ 50 mN m^{-1}. Ovadnevaite et al. (2017) suggested that LLPS leads to complete or partial engulfing of a hygroscopic particle core by a hydrophobic organic-rich phase. This results in substantial decrease of surface tension without a reduction of the Raoult's effect, leading to higher CCN activity. Simulations based on this LLPS model suggest the effect of reduced surface tension on CCN activity is more pronounced for ultrafine particles, and the effect is much weaker for particles with larger diameters studied here. One prediction of the model is that particles with different organics to sulfate mass ratios (i.e.

sulfate volume fraction) exhibit similar effective hygroscopicity parameter. Such behavior is explained by that a decrease in sulfate content, and therefore the Raoult's effect, is compensated for by a prolonged surface tension lowering (to larger diameters during droplet activation) due to a larger relative amount of organics (Ovadnevaite et al., 2017). This trend is very different from the results of SOA examined in this study, which show a nearly constant κ_{org} therefore lower effective hygroscopicity parameter for particles with high organics to sulfate mass ratio.

Ruehl et al. (2016) measured droplet diameters at the point of CCN activation for particles composed of dicarboxylic acids or SOA and ammonium sulfate. They found that critical droplet diameters were 40 to 60% larger than predicted if the organic was assumed to be dissolved within the bulk droplet. The larger critical droplet diameter was attributed to surface tension depression by interfacial organic molecules, which can alter the relationship between water vapor supersaturation and droplet size (i.e., the Köhler curve). The same experiment approach was recently applied by Forestieri et al. (2018) to systems resembling those of marine aerosol. The results show that while surface tension depression by interfacial organic molecules may strongly influence the shape of Köhler curve, the net effect on critical supersaturation, and therefore effective hygroscopicity is generally minor. Therefore, until evidence is presented to the contrary, we expect that exact compensation between solubility limitations and an interfacial mechanism resulting in constant κ_{org} vs. x_{AS} for the SOA examined in this study is unlikely.

Table S1. Conditions of the steady state chamber experiments in this study. Also listed are the values of κ_{org}, O:C, and H:C for each experiment. Reactant concentrations in the inflow of the chamber air are listed. Unless otherwise noted, experiments were conducted with UV lights on and at 50% RH.

Exp. Date	Experiment condition	κ_{org}	O:C	H:C
6/21/2015	α-pinene 10 ppb, H_2O_2 5 ppm	0.10	0.55	1.8
6/22/2015	α-pinene 10 ppb, H_2O_2 0.5 ppm	0.10	0.52	1.72
6/25/2016	Δ-3 carene 10 ppb, H_2O_2 0.5 ppm	0.10	0.53	1.76
6/26/2015	Δ-3 carene 10 ppb, H_2O_2 0.25 ppm	0.10	0.54	1.75
6/27/2015	α-pinene 10 ppb, H_2O_2 1 ppm	0.10	0.5	1.74
7/1/2015	α-pinene 10 ppb, H_2O_2 1 ppm, NO 5 ppb	0.10	0.5	1.69
7/2/2015	α-pinene 10 ppb, H_2O_2 1 ppm, NO 10 ppb	0.11	0.53	1.67
7/3/2015	α-pinene 10 ppb, H_2O_2 1 ppm, NO 25 ppb	0.11	0.57	1.63
7/7/2015	α-pinene 20 ppb, H_2O_2 1 ppm, O_3 60 ppb	0.10	0.44	1.69
7/8/2015	α-pinene 20 ppb, H_2O_2 1 ppm, O_3 60 ppb, 2×residence time[a]	0.10	0.44	1.69
7/12/2015	α-pinene 10 ppb, H_2O_2 5 ppm, O_3 80 ppb, dark	0.10	0.59	1.63
7/14/2015	α-pinene 10 ppb, cyclohexane 10 ppm, O_3 80 ppb, NO 25 ppb	0.11	0.61	1.65
9/2/2015	Isoprene 15 ppb, H_2O_2 5 ppm	0.16	0.87	2.13
2/14/2016	β-caryophyllene, H_2O_2 1 ppm, <5% RH;	0.07[b]	0.33	1.72
2/22/2016	Toluene 110 ppb, H_2O_2 5 ppm, <5% RH;	0.13	0.87	1.57

[a] Mean residence time increased to 7.4 hours.

[b] Average value when sulfate volume fraction is greater than 15% (i.e., when droplet activation is not limited by the water solubility of β-caryophyllene SOA.)

Table S2. Equations used in the model for predicting effective hygroscopicity of organic surfactants with limited solubility (Petters and Kreidenweis, 2008, 2013).

Equation	**Description**
$A = \pi D^2$	Surface area of droplet
$V = \frac{\pi}{6} D^3$	Volume of entire droplet
$V_s^t = \frac{\pi}{6} D_d^3$	Volume of dry particle
$g = \frac{D}{D_d}$	Growth factor
$f_{sft} = C(g^3 - 1)\epsilon_{sft}^{-1}$	Fraction of surfactant dissolved based on bulk solubility ($f_{sft} = [0..1]$)
$V_{sft} = f_{sft}\epsilon_{sft}V_s^t$	Volume of surfactant dissolved in the droplet
$V_{sft}^b = \frac{\alpha_{sft}(g + \sqrt{g^2 + 4\varepsilon_{sft}V_s^t \beta V / \alpha_{sft}})}{2}$ $g = \frac{\varepsilon_{sft}V_s^t}{\alpha_{sft}} - \beta V - \frac{A\Gamma_{\max}}{\nu}$	Volume fraction of dissolved surfactant in the bulk based on approximation described in Raatikainen and Laaksonen (2011).
$\sigma_{s/a} = \sigma_0 - RT\Gamma_{\max} \ln\left(1 + \frac{V_{sft}^b}{\alpha_{sft}\beta V}\right)$ $\sigma_{s/a} = \sigma_{cmc}$ if $\sigma_{s/a}$ evaluates too low	Sorption isotherm from Szyskowski equation based on bulk dissolved surfactant
$\xi = \frac{V_{sft}^b}{V_{sft}}$	Surface/bulk partitioning fraction
$\kappa = \epsilon_{sft}\xi f_{sft}\kappa_{sft} + (1 - \epsilon_{sft})\kappa_{core}$	Kappa mixing rule accounting for solubility and surface partitioning. Note that for no surfactant partitioning and infinite solubility $\xi = 1$ and $f_{sft} = 1$.
$S(D) = \frac{D^3 - D_d^3}{D^3 - D_d^3(1-\kappa)} \exp\left(\frac{A\sigma_{s/a}}{TD}\right)$	The equation from which S_c is determined and κ_{org} is inferred.

Table S3. Key parameters of the model used to predict effective hygroscopicity of organic surfactants with limited solubility (Petters and Kreidenweis, 2008, 2013). Assumed quantities are marked in red.

Parameter	Description
$D_d\ (m)$	Dry particle diameter (assumed)
$D\ (m)$	Wet droplet diameter (derived)
$A\ (m^2)$	Wet surface area (derived)
$V\ (m^3)$	Wet particle volume (derived)
$V_s^t\ (m^3)$	Dry particle volume (derived)
$g\ (-)$	Growth factor (derived)
$\Gamma_{max}\ (mol\ m^{-2})$	Maximum surface excess (assumed)
$\beta\ (mol\ m^{-3})$	Inverse activity coefficient (assumed)
$C\ \left(\frac{m^3\ solute}{m^3\ water}\right)$	Solubility in water (assumed)
$\alpha\ (m^3\ mol^{-1})$	Molar volume of surfactant (assumed)
$\kappa_{sft}\ (-)$	κ of surfactant (assumed or derived from α)
$\kappa_{core}\ (-)$	κ of the ammonium sulfate core (assumed $\kappa_{core} = 0.6$)
$\epsilon_{sft}\ (-)$	Volume fraction of surfactant in dry particle. Calculated from core diameter (50 nm) and total particle diameter.
$\sigma_{cmc}\ (J\ m^{-2})$	Lowest allowed surface tension (assumed)

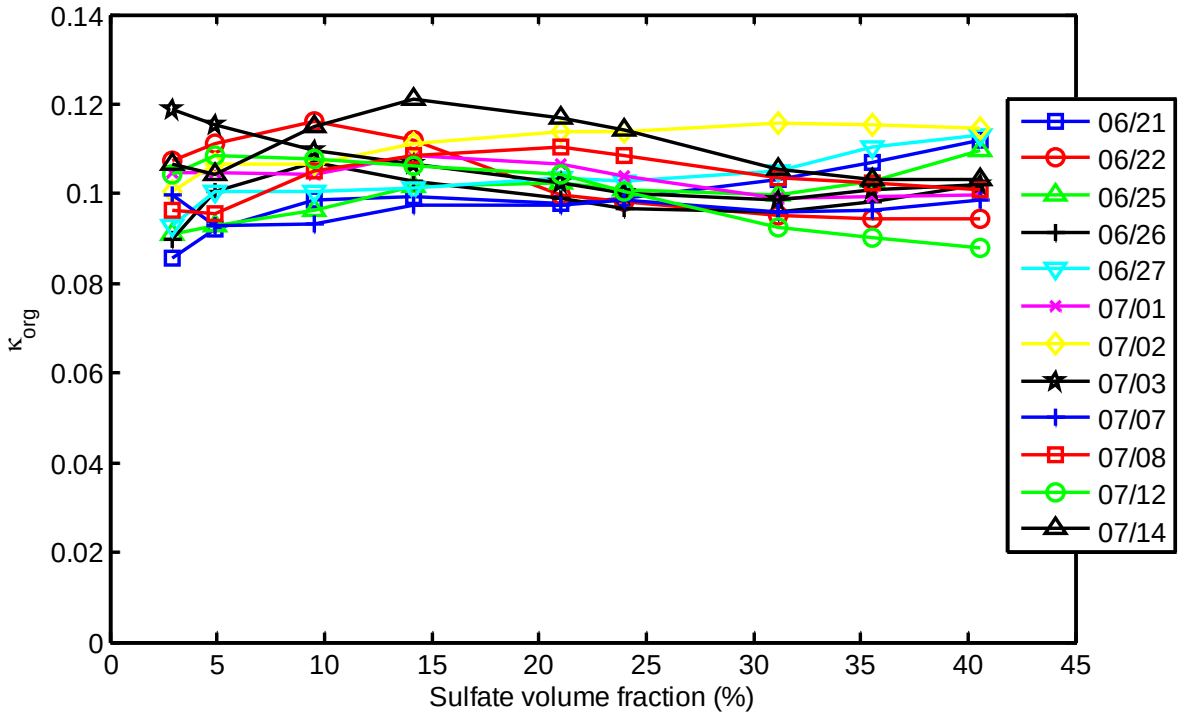

Figure S1. Effective organic hygroscopicity as a function of particle sulfate volume fraction for secondary organic aerosols formed from α-pinene and Δ-3 carene under a variety of conditions. The legend refers to the experiment date. The condition for each experiment is detailed in Table S1.

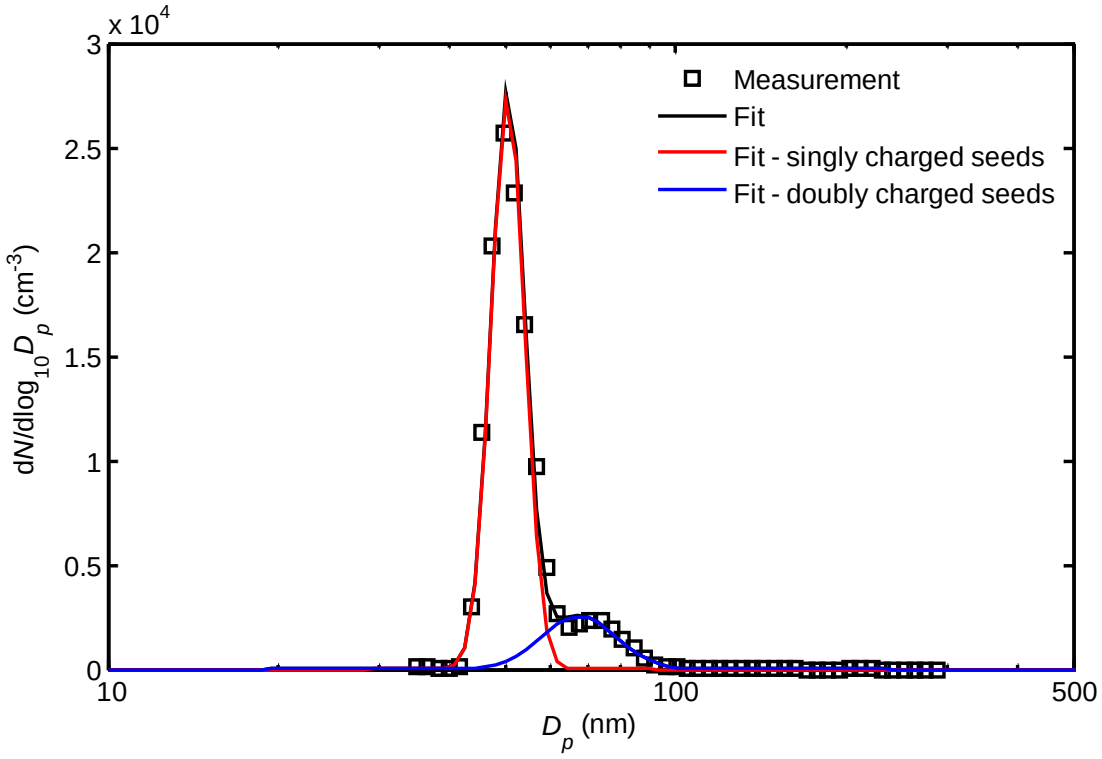

Figure S2. An example of measured size distribution of ammonium sulfate seeds. Also shown are the lognormal fits of all, singly-charged, and doubly charged seeds.

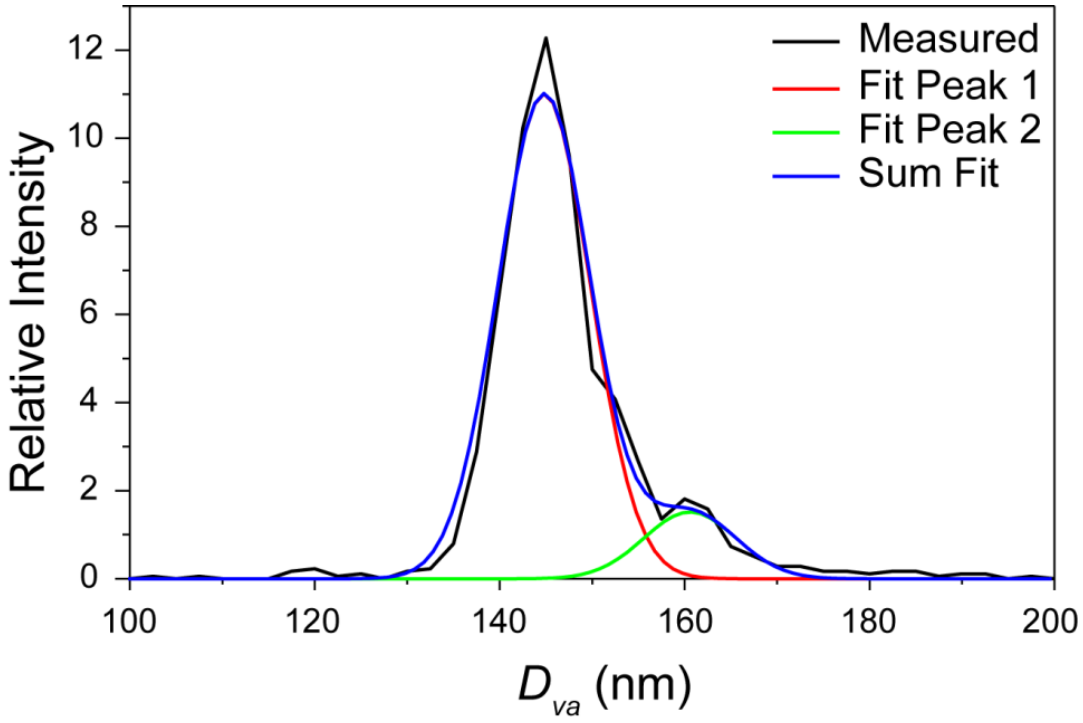

Figure S3. An example D_{va} distributions of 100 nm SOA-coated AS particles classified by a DMA during the experiment on June 21, 2015. Also shown are fitted peaks corresponding to particles grown on singly and doubly charged AS seeds, respectively.

5

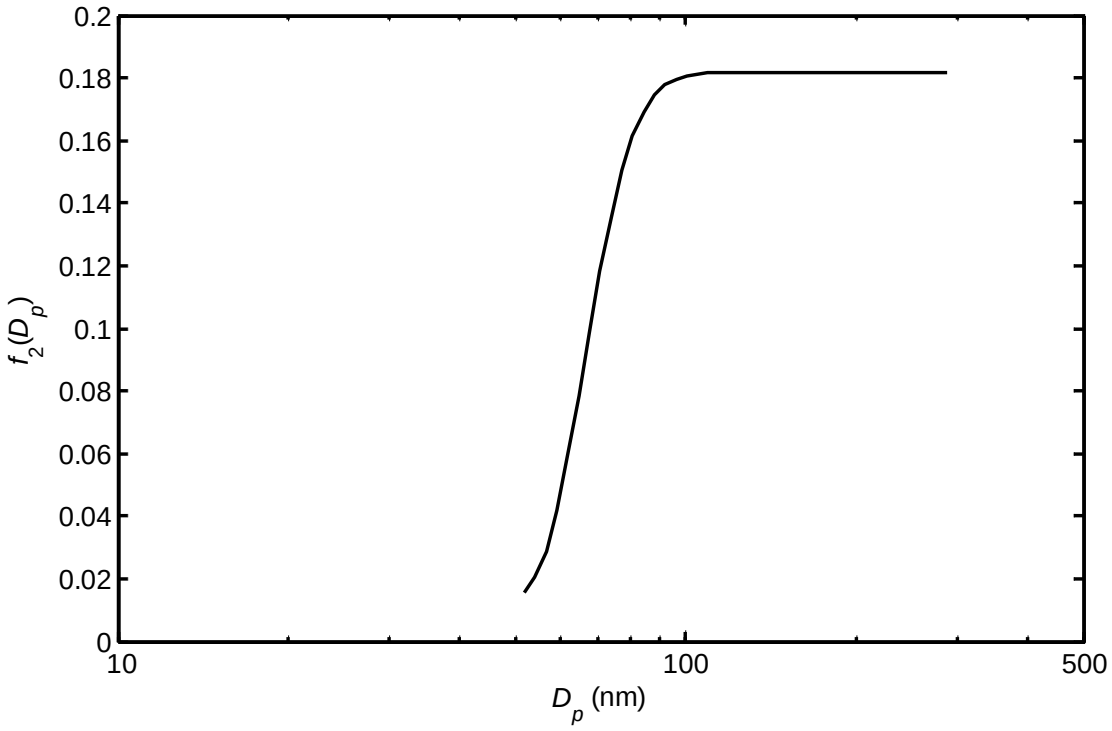

Figure S4. The value of $f_2(D_p)$ as a function of D_p derived from seed particle size distributions using τ of 4.3 hours, and a set of representative parameters (i.e., $\alpha = 0.027\ h^{-1}$, β_A=1.5 e-6 $\mu m^2 s^{-1}$, β_B=2.5 e-7 $\mu m^2 s^{-1}$, λ_A = 17 nm, and λ_A = 21 nm) reported in Seinfeld et al. (2003)

5

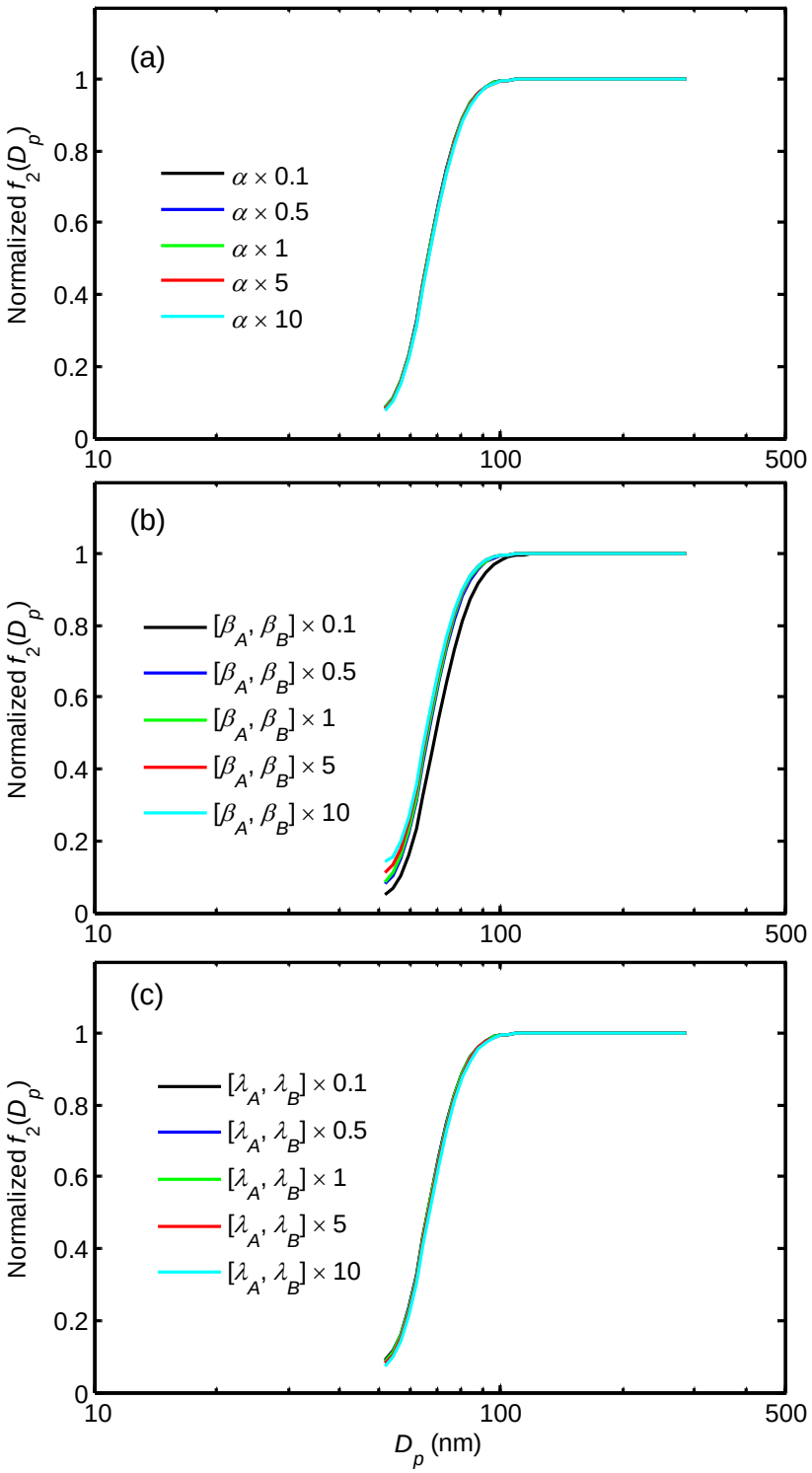

Figure S5: The dependences of $\overline{f_2(D_p)}$ on values of (a) α, (b) β_i, and (c) λ_i , respectively.

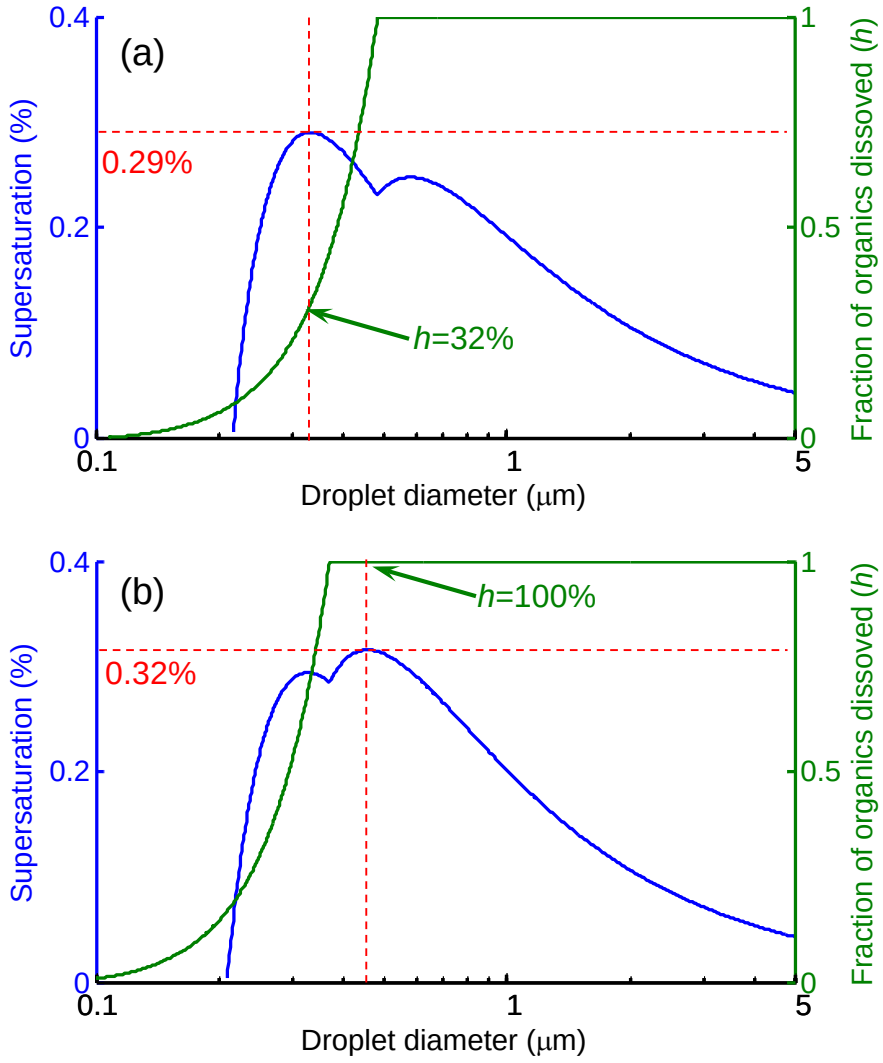

Figure S6: Example of calculated Köhler curve (blue line) for particles consisting of sulfate and sparing soluble organics with solubility of 0.01. The volume of sulfate inside the particles is equivalent to a 50 nm sulfate particle and the sulfate volume fractions are 0.1 (a) and 0.2 (b) respectively. Also shown is the fraction of organics dissolved (*h*) as a function of droplet diameter, the critical supersaturation (i.e., peak of the Köhler curve) and the corresponding *h*.

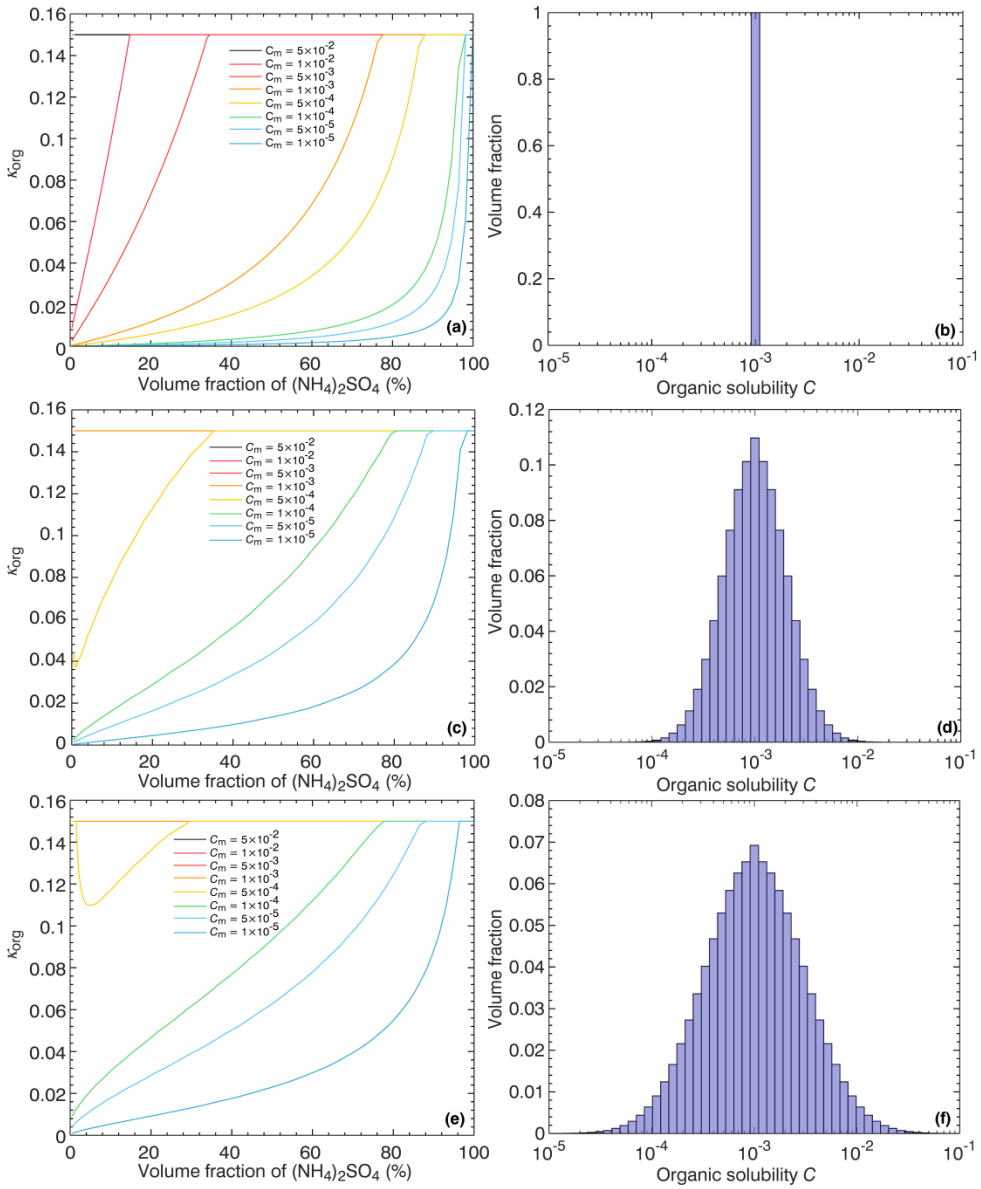

Figure S7. Panels (a), (c), and (e): Simulated effective organic hygroscopicity for particles grown from 50 nm ammonium sulfate seeds by condensation of secondary organic species with $\kappa_{org,intr}$ = 0.15. The effective organic hygroscopicity is shown as a function of sulfate volume fraction for organic solubility distributions C with mode solubility (C_m) ranging from 5×10^{-2} to 1×10^{-5}. Panels (b), (d), and (f): examples of solubility distribution centered at $C_m = 1\times10^{-3}$ for the 61 component mixture.

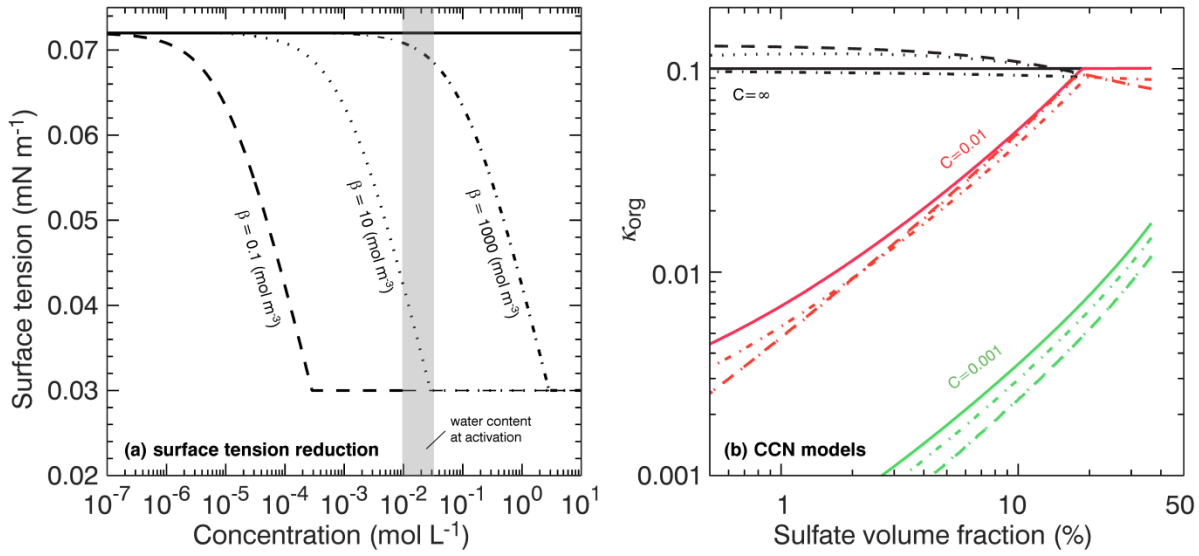

Figure S8. Model calculations combining limited solubility and surface tension reduction. (a) Hypothetical Szyskowski surface tension isotherms assuming $\alpha = 1.8 \times 10^{-4}\, m^3\, mol^{-1}$, $\Gamma_{max} = 5 \times 10^{-6}\, mol\, m^{-2}$, $\beta = \{0.1, 10, 1000\}\, mol\, m^{-3}$, and $cmc = 0.03\, J\, m^{-2}$. (b) Modeled κ_{org} assuming $C = \{\infty, 0.01,\ 0.001\}$ (colors). Solid line corresponds to constant surface tension $\sigma = 0.072\, J\, m^{-2}$. Dashed and dotted lines assume surface tension reduction as shown in (a).

References in Supplementary Information:

Allan, J. D., Delia, A. E., Coe, H., Bower, K. N., Alfarra, M. R., Jimenez, J. L., Middlebrook, A. M., Drewnick, F., Onasch, T. B., Canagaratna, M. R., Jayne, J. T., and Worsnop, D. R.: A generalised method for the extraction of chemically resolved mass spectra from aerodyne aerosol mass spectrometer data, J. Aerosol Sci., 35, 909-922, 2004.

Asa-Awuku, A., Engelhart, G. J., Lee, B. H., Pandis, S. N., and Nenes, A.: Relating CCN activity, volatility, and droplet growth kinetics of beta-caryophyllene secondary organic aerosol, Atmos. Chem. Phys., 9, 795-812, 2009.

Bertram, A. K., Martin, S. T., Hanna, S. J., Smith, M. L., Bodsworth, A., Chen, Q., Kuwata, M., Liu, A., You, Y., and Zorn, S. R.: Predicting the relative humidities of liquid-liquid phase separation, efflorescence, and deliquescence of mixed particles of ammonium sulfate, organic material, and water using the organic-to-sulfate mass ratio of the particle and the oxygen-to-carbon elemental ratio of the organic component, Atmos. Chem. Phys., 11, 10995-11006, 2011.

Bilde, M. and Svenningsson, B.: CCN activation of slightly soluble organics: the importance of small amounts of inorganic salt and particle phase, Tellus B, 56, 128-134, 2004.

Canagaratna, M. R., Jimenez, J. L., Kroll, J. H., Chen, Q., Kessler, S. H., Massoli, P., Hildebrandt Ruiz, L., Fortner, E., Williams, L. R., Wilson, K. R., Surratt, J. D., Donahue, N. M., Jayne, J. T., and Worsnop, D. R.: Elemental ratio measurements of organic compounds using aerosol mass spectrometry: characterization, improved calibration, and implications, Atmos. Chem. Phys., 15, 253-272, 2015.

Chen, Q., Liu, Y. J., Donahue, N. M., Shilling, J. E., and Martin, S. T.: Particle-Phase Chemistry of Secondary Organic Material: Modeled Compared to Measured O:C and H:C Elemental Ratios Provide Constraints, Environ. Sci. Technol., 45, 4763-4770, 2011.

Collins, D. R., Flagan, R. C., and Seinfeld, J. H.: Improved inversion of scanning DMA data, Aerosol Sci. Technol., 36, 1-9, 2002.

DeCarlo, P. F., Kimmel, J. R., Trimborn, A., Northway, M. J., Jayne, J. T., Aiken, A. C., Gonin, M., Fuhrer, K., Horvath, T., Docherty, K., Worsnop, D. R., and Jimenez, J. L.: Field-Deployable, High-Resolution, Time-of-Flight Aerosol Mass Spectrometer, Anal. Chem., 78, 8281-8289, 2006.

Forestieri, S. D., Staudt, S. M., Kuborn, T. M., Faber, K., Ruehl, C. R., Bertram, T. H., and Cappa, C. D.: Establishing the Impact of Model Surfactants on Cloud Condensation Nuclei Activity of Sea Spray Aerosols, Atmos. Chem. Phys. Discuss., 2018. https://doi.org/10.5194/acp-2018-5207, 2018.

Holmes, J. R., Obrien, R. J., Crabtree, J. H., Hecht, T. A., and Seinfeld, J. H.: MEASUREMENT OF ULTRAVIOLET-RADIATION INTENSITY IN PHOTOCHEMICAL SMOG STUDIES, Environ. Sci. Technol., 7, 519-523, 1973.

Hori, M., Ohta, S., Murao, N., and Yamagata, S.: Activation capability of water soluble organic substances as CCN, J. Aerosol Sci., 34, 419-448, 2003.

Kuwata, M., Zorn, S. R., and Martin, S. T.: Using Elemental Ratios to Predict the Density of Organic Material Composed of Carbon, Hydrogen, and Oxygen, Environ. Sci. Technol., 46, 787-794, 2012.

Lindinger, W., Hansel, A., and Jordan, A.: On-line monitoring of volatile organic compounds at pptv levels by means of proton-transfer-reaction mass spectrometry (PTR-MS) - Medical applications, food control and environmental research, International Journal of Mass Spectrometry, 173, 191-241, 1998.

Mei, F., Setyan, A., Zhang, Q., and Wang, J.: CCN activity of organic aerosols observed downwind of urban emissions during CARES, Atmos. Chem. Phys., 13, 12155-12169, 2013.

Noziere, B., Baduel, C., and Jaffrezo, J. L.: The dynamic surface tension of atmospheric aerosol surfactants reveals new aspects of cloud activation, Nature Communications, 5, 2014.

Ovadnevaite, J., Zuend, A., Laaksonen, A., Sanchez, K. J., Roberts, G., Ceburnis, D., Decesari, S., Rinaldi, M., Hodas, N., Facchini, M. C., Seinfeld, J. H., and Dowd, C. O.: Surface tension prevails over solute effect in organic-influenced cloud droplet activation, Nature, 546, 637-641, 2017.

Petters, M. D. and Kreidenweis, S. M.: A single parameter representation of hygroscopic growth and cloud condensation nucleus activity - Part 2: Including solubility, Atmos. Chem. Phys., 8, 6273-6279, 2008.

Petters, M. D. and Kreidenweis, S. M.: A single parameter representation of hygroscopic growth and cloud condensation nucleus activity - Part 3: Including surfactant partitioning, Atmos. Chem. Phys., 13, 1081-1091, 2013.

Petters, M. D., Kreidenweis, S. M., Snider, J. R., Koehler, K. A., Wang, Q., Prenni, A. J., and Demott, P. J.: Cloud droplet activation of polymerized organic aerosol, Tellus B, 58, 196-205, 2006.

Petters, M. D., Kreidenweis, S. M., and Ziemann, P. J.: Prediction of cloud condensation nuclei activity for organic compounds using functional group contribution methods, Geosci. Model Dev., 9, 111-124, 2016.

Petters, S. S. and Petters, M. D.: Surfactant effect on cloud condensation nuclei for two-component internally mixed aerosols, J. Geophys. Res., 121, 1878-1895, 2016.

Prisle, N. L., Raatikainen, T., Laaksonen, A., and Bilde, M.: Surfactants in cloud droplet activation: mixed organic-inorganic particles, Atmos. Chem. Phys., 10, 5663-5683, 2010.

Raatikainen, T. and Laaksonen, A.: A simplified treatment of surfactant effects on cloud drop activation, Geosci. Model Dev., 4, 107-116, 2011.

Rothfuss, N. E. and Petters, M. D.: Influence of Functional Groups on the Viscosity of Organic Aerosol, Environ. Sci. Technol., 51, 271-279, 2017.

Ruehl, C. R., Davies, J. F., and Wilson, K. R.: An interfacial mechanism for cloud droplet formation on organic aerosols, Science, 351, 1447-1450, 2016.

Seinfeld, J. H., Kleindienst, T. E., Edney, E. O., and Cohen, J. B.: Aerosol growth in a steady-state, continuous flow chamber: Application to studies of secondary aerosol formation, Aerosol Sci. Technol., 37, 728-734, 2003.

Shulman, M. L., Jacobson, M. C., Carlson, R. J., Synovec, R. E., and Young, T. E.: Dissolution behavior and surface tension effects of organic compounds in nucleating cloud droplets, Geophys. Res. Lett., 23, 277-280, 1996.

Topping, D., Connolly, P., and McFiggans, G.: Cloud droplet number enhanced by co-condensation of organic vapours, Nature Geoscience, 6, 443-446, 2013.

Zelenyuk, A., Imre, D., Wilson, J., Zhang, Z., Wang, J., and Mueller, K.: Airborne Single Particle Mass Spectrometers (SPLAT II & miniSPLAT) and New Software for Data Visualization and Analysis in a Geo-Spatial Context, Journal of The American Society for Mass Spectrometry, 26, 257-270, 2015.

Zelenyuk, A., Yang, J., Song, C., Zaveri, R. A., and Imre, D.: A New Real-Time Method for Determining Particles' Sphericity and Density: Application to Secondary Organic Aerosol Formed by Ozonolysis of α-Pinene, Environmental Science & Technology, 42, 8033-8038, 2008a.

Zelenyuk, A., Yang, J., Song, C., Zaveri, R. A., and Imre, D.: A New Real-Time Method for Determining Particles' Sphericity and Density: Application to Secondary Organic Aerosol Formed by Ozonolysis of alpha-Pinene, Environ. Sci. Technol., 42, 8033-8038, 2008b.